Series of phase transitions and multiferroicity in the quasi-two-dimensional spin-$\frac{1}{2}$ triangular-lattice antiferromagnet $Ba_3CoNb_2O_9$

M. Lee,[1,2] J. Hwang,[1,2] E. S. Choi,[2,*] J. Ma,[3] C. R. Dela Cruz,[3] M. Zhu,[4] X. Ke,[4] Z. L. Dun,[5] and H. D. Zhou[5,2,†]

[1]*Department of Physics, Florida State University, Tallahassee, Florida 32306-3016, USA*

[2]*National High Magnetic Field Laboratory, Florida State University, Tallahassee, Florida 32310-3706, USA*

[3]*Quantum Condensed Matter Division, Oak Ridge National Laboratory, Oak Ridge, Tennessee 37381, USA*

[4]*Department of Physics and Astronomy, Michigan State University, East Lansing, Michigan 48824, USA*

[5]*Department of Physics and Astronomy, University of Tennessee, Knoxville, Tennessee 37996-1200, USA*

(Received 19 August 2013; revised manuscript received 3 February 2014; published 24 March 2014)

We have investigated the magnetic and electric ground states of a quasi-two-dimensional triangular lattice antiferromagnet (TLAF), $Ba_3CoNb_2O_9$, in which the effective spin of Co^{2+} is 1/2. At zero field, the system undergoes a two-step transition upon cooling at $T_{N2} = 1.36$ K and $T_{N1} = 1.10$ K and enters a 120° ordered state. By applying magnetic fields, a series of spin states with fractions of the saturation magnetization M_s are observed. They are spin states with 1/3, 1/2, 2/3 (or $\sqrt{3}/3$) M_s. The ferroelectricity emerges in all spin states, either with collinear or noncollinear spin structure, which makes $Ba_3CoNb_2O_9$ another unique TLAF exhibiting both a series of magnetic phase transitions and multiferroicity. We discuss the role of quantum fluctuations and magnetic anisotropy in contributing more complex phase diagram compared to its sister multiferroic TLAF compound $Ba_3NiNb_2O_9$ [J. Hwang *et al.*, Phys. Rev. Lett. **109**, 257205 (2012)].

DOI: 10.1103/PhysRevB.89.104420 PACS number(s): 75.40.Cx, 75.10.Jm, 75.85.+t, 77.22.Ej

I. INTRODUCTION

The geometrical frustration and spin fluctuation in magnets can lead to many exotic properties at low temperatures such as quantum spin liquid, spin ice, and magnetization plateau [1]. The realization of a quantum spin system with the simplest form of geometrical frustration can be achieved in a two-dimensional (2D) triangular lattice antiferromagnet (TLAF) with small spins ($S = 1/2$ or 1) [2]. For example, in $Ba_3CoSb_2O_9$ [3–5] and $Ba_3CoNb_2O_9$ (in this work) compounds, the magnetic ions (Co^{2+} with effective spin $S = 1/2$ at low temperatures) lie on 2D regular triangular lattice planes well separated by nonmagnetic layers. In TLAFs with Heisenberg spins, the spins order antiferromagnetically forming 120° spin structure at zero magnetic field. Theories predicted that the 120° ordered state evolves to different magnetically ordered states under magnetic field, first to an "up-up-down" (*uud*) state with total moment equal to 1/3 of the saturation magnetization M_s [6–8]. The *uud* state can be stabilized over a wide range of field, hence showing a magnetization plateau, through quantum and/or thermal fluctuations. By applying higher magnetic fields, the *uud* state becomes energetically unstable yielding to 2:1 canted spin states.

Experimentally, the 1/3 magnetization plateau has been observed in TLAFs with a regular triangular lattice ($RbFe(MoO_4)_2$ ($S = 5/2$) [9], $Rb_4Mn(MoO_4)_3$ ($S = 5/2$) [10], $Ba_3NiSb_2O_9$ ($S = 1$) [11], $Ba_3NiNb_2O_9$ [12], $Ba_3CoSb_2O_9$ ($S = 1/2$) [3–5]) and with an isosceles triangular lattice [Cs_2CuBr_4 ($S = 1/2$)] [13,14]. More interestingly, the recent studies reveal that quantum spin fluctuations may stabilize more quantum spin states with higher fractions of M_s under fields in TLAFs with $S = 1/2$. For example, Cs_2CuBr_4 shows extra spin states with 1/2, 5/9, and 2/3 M_s [14], $Ba_3CoSb_2O_9$ shows a spin state with 3/5 M_s [4], and $Ba_3NiNb_2O_9$ shows a 2:1 canted spin sate with $\sqrt{3}/3$ M_s [12]. All these spin states have not been predicted theoretically and fully understood. Searching for new TLAFs with quantum spin states is still a very active topic in condensed matter physics.

Multiferroicity, where more than one ferroic order coexists in the same phase, is another interesting property discovered in TLAFs. In magnetoelectric multiferroics, the magnetic and electric degrees of freedom are strongly coupled [15,16], which may be utilized for new types of memory devices [17,18]. In TLAFs with classical spins, $RbFe(MoO_4)_2$ [19] and $ACrO_2$ ($S = 3/2$, A = Ag and Cu) [20,21] have shown multiferroicity in the magnetic phase where the spins have noncollinear spin structures. Although the exact mechanism of the multiferroicity in TLAFs is still under development [22], the spin chirality is likely to play a crucial role considering the disappearance of the ferroelectricity in the *uud* state. On the other hand, our recent studies on $Ba_3NiNb_2O_9$ show that the ferroelectricity persists in the collinear spin states (*uud* and 2:1 canted spin state), and coexists with the quantum spin states [12], which adds complexity to the existing understanding of the multiferroicity in TLAFs.

In this paper, we extended our studies to another new TLAF, $Ba_3CoNb_2O_9$. Based on specific heat, neutron diffraction, dc susceptibility and magnetization, ac susceptibility, dielectric constant, and polarization experiments, a detailed H-T phase diagram is constructed for $Ba_3CoNb_2O_9$. The complex phase diagram reveals a series of spin states with 1/3, 1/2, 2/3 (or $\sqrt{3}/3$) M_s under fields, and another possible spin state at lower fields between the 120° phase and the *uud* phase with 1/3 M_s. At zero field, it goes through a two-step transition to enter the 120° spin ordered state. The phase diagram also shows that the multiferroicity is present in both noncollinear and all collinear spin states. These results demonstrate that $Ba_3CoNb_2O_9$ is another rare TLAF with S-1/2 in which the quantum spin fluctuations lead to a series of spin states and they coexist with the ferroelectricity.

*echoi@magnet.fsu.edu

†hzhou10@utk.edu

The rest of the paper is organized as follows. In Sec. II, the sample preparation and experimental setups are described. In Sec. III, we report experimental results: (i) first low- or zero-magnetic field data of dc magnetic susceptibility, specific heat, and neutron powder diffraction, and (ii) high-field magnetization, ac susceptibility, dielectric constant, and electric polarization measurements. Finally, in Sec. IV, we present the H-T phase diagram and discuss our experimental results.

II. EXPERIMENTAL

Polycrystalline samples of $Ba_3CoNb_2O_9$ were made by solid state reaction. Appropriate mixtures of $BaCO_3$, $CoCO_3$, and Nb_2O_5 were ground together, pressed into pellets, and then calcined in air at 1230 °C for 24 hours. The room temperature x-ray diffraction pattern confirms its trigonal P-3m1 space group with $a = 5.7737(4)$ Å and $c = 7.0852(5)$ Å, which agrees very well with a previous report [23]. $Ba_3CoNb_2O_9$ is isostructural to $Ba_3NiNb_2O_9$ and can be represented as a framework consisting of corner-sharing CoO_6 and NbO_6 octahedra. The Co ions occupy the 1b Wyckoff sites and forms the triangular lattice in the ab plane. Its structure can be regarded as a pseudo-two-dimensional triangular magnet; i.e., the Co magnetic triangular lattices are magnetically separated by the two nonmagnetic Nb layers. For structural details, see Ref. [12].

The dc magnetization measurements were performed with a high-field vibrating sample magnetometer (VSM) of the National High Magnetic Field Laboratory and with a commercial SQUID magnetometer (magnetic property measurement system, Quantum Design). The ac susceptibility measurement was done with a home-made ac susceptometer. The specific heat was measured with the physical property measurement system by Quantum Design. The neutron diffraction measurements were performed below 1.7 K by using the neutron powder diffractometer HB2A at ORNL with the wavelength of 2.41 Å.

For the dielectric constant and the polarization measurement, samples were polished to have a parallel capacitor geometry with typical dimensions of $10 \times 5 \times 0.2$ mm^3. The electrical contacts were made by painting silver epoxy on the two parallel opposite surfaces. The dielectric constant was measured with an Andeen-Hagerling AH-2700A capacitance bridge. The polarization was obtained by integrating the pyroelectric current signal as a function of time. For the pyroelectric current measurement, the following procedures were taken. (1) A sample was cooled down through a transition under different conditions of electric and magnetic field, (2) the electric field was removed and the sample was short circuited for 15 minutes to remove the residual surface charge, (3) the magnetic field was set to a desired value if the sample had been cooled down without magnetic field, and (4) the transient current was measured with a Keithley 6517A electrometer upon warming.

III. RESULTS

A. dc magnetic susceptibility and specific heat

The inverse of the dc magnetic susceptibility ($\chi = M/H$) above 1.8 K for $Ba_3CoNb_2O_9$ is shown in Fig. 1(a). A change of slope for $1/\chi$ is observed at around 50 K. The

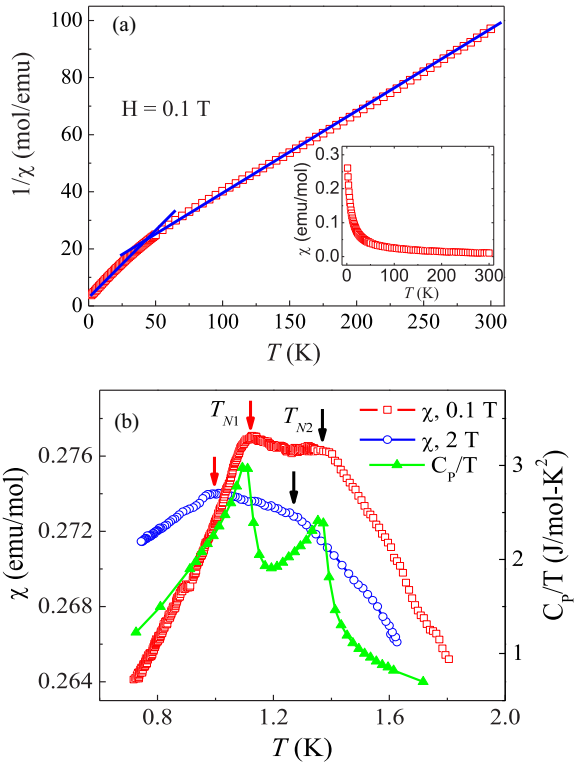

FIG. 1. (Color online) (a) The temperature dependence of the inverse of the dc magnetic susceptibility. The symbols are experimental data and the solid lines are linear fittings. Inset: dc magnetic susceptibility. (b) The low-temperature dc magnetic susceptibility and specific heat.

effective moment is estimated to be 5.3 μ_B for 100 K $< T <$ 300 K and 4.0 μ_B for 2 K $< T <$ 20 K by using the linear Curie-Weiss fittings. This decrease of effective moment indicates a crossover of spin state for Co^{2+} from high ($S = 3/2$) to low ($S = 1/2$) spin state. For Co^{2+} ions in an octahedral environment, as for $Ba_3CoNb_2O_9$, the crystal field and spin-orbital coupling leads to a Kramers doublet with the effective spin-1/2 as the ground state. For other TLAFs with octahedral Co sites, such as $Ba_3CoSb_2O_9$ [24] and $ACoB_3$ (A = Cs, Rb, B = Cl, Br) [25], the ground state is also with effective spin-1/2. The estimated 4.0 μ_B lies between 1.7 (spin only) and 4.5 μ_B (with full angular momentum contribution) for a S-1/2 state. It is therefore reasonable to assume an effective S-1/2 state for Co^{2+} in $Ba_3CoNb_2O_9$ at low temperatures.

At lower temperatures, χ was measured by the VSM, of which the data are presented in Fig. 1(b). The VSM data show two kinks at T_{N1} and T_{N2} ($T_{N1} < T_{N2}$) characterized as a broad peak or a shoulder at T_{N2} and a decrease of susceptibility below T_{N1}. Both T_{N1} and T_{N2} decrease and the features become broader with increasing magnetic fields. Specific heat was measured to investigate the nature of the susceptibility kinks at zero field, whose result is shown in Fig. 1(b). There are two sharp peaks at $T_{N2} = 1.36$ K and $T_{N1} = 1.10$ K, which indicates the susceptibility kinks are from long-range magnetic orderings. The fact that the susceptibility decreases below T_{N1} suggests an antiferromagnetic (AFM) ordering.

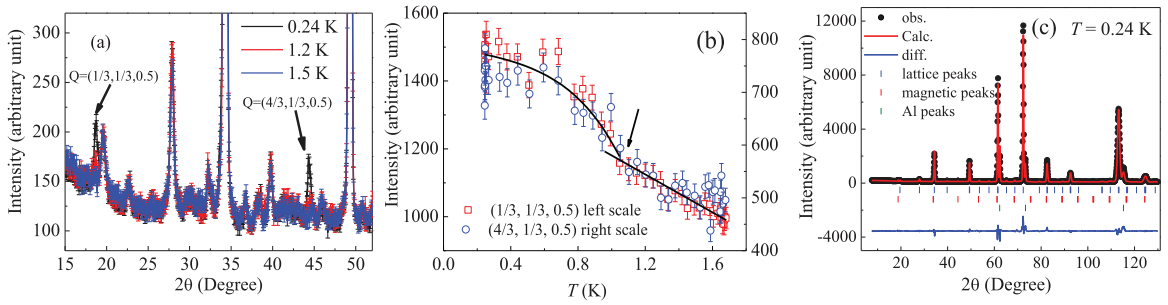

FIG. 2. (Color online) (a) The neutron powder diffraction (NPD) patterns taken at $T = 0.24$, 1.2, and 1.5 K (b) The temperature dependence of the intensity (area of the peak) of the magnetic Bragg peaks at $Q = (1/3, 1/3, 0.5)$ and $(4/3, 1/3, 0.5)$. The symbols are experimental data and the solid lines are guide to eyes. (c) NPD pattern taken at $T = 0.24$ K. The solid curve is the best fit from the Rietveld refinement by using FULLPROF.

B. Neutron powder diffraction

Neutron powder diffraction experiments were performed in order to identify the magnetic structures at low temperatures at zero field. The NPD data taken at three different temperatures are shown in Fig. 2(a). While the lattice Bragg peaks do not show temperature dependence, two magnetic Bragg peaks with $Q = (1/3, 1/3, 0.5)$ and $(4/3, 1/3, 0.5)$ are clearly observed at $T = 0.24$ K, which are absent at $T = 1.5$ K. The temperature dependence of the order parameter [area of the $(1/3, 1/3, 0.5)$ and $(4/3, 1/3, 0.5)$ peaks] shows a rapid increase at $T = 1.0$ K, close to T_{N1}, while there is no obvious feature around T_{N2} [Fig. 2(b)].

The Rietveld refinement of the 0.24 K pattern [Fig. 2(c)] revealed the same lattice structure (P-3m1) at low temperatures suggesting no obvious structural distortion down to 0.24 K. Since only two magnetic peaks were observed, it is difficult to determine magnetic structure exclusively. Among possible magnetic space groups, P-1 gave good refinement results, which is a magnetic structure with collinear antiferromagnetic (AFM) spins between the nearest-neighbor layers and a 120° AFM spin ordering. This magnetic structure is consistent with the decrease of χ below T_{N1} and is the same as that of $Ba_3NiNb_2O_9$ [12].

The ordered moment is fitted to be 0.97(1) μ_B for each Co^{2+} ion, which further confirms the S-1/2 spin state for Co^{2+} at low temperatures. Due to the resolution limit, the refinement cannot tell whether the 120° ordered spins lie in the ab plane or in a plane containing the c axis (an easy-axis type 120° structure). In addition, there is an unidentified peak around 22.5° with no temperature dependence, which is probably due to a small percentage of unidentified impurity. Further NPD experiments probably on single-crystal samples with better resolution will resolve the issues of the unidentified peak as well as more definitive determination of the magnetic structure. In Table I, we summarize the structural and magnetic parameters obtained from the $T = 0.24$ K NPD data.

C. dc magnetization and ac susceptibility

Figure 3 shows the dc magnetization data $[M(H)]$ at $T = 0.64$ K measured with the high-field vibrating VSM at NHMFL. The Co^{2+} spin saturates at $H_s = 5$ T, above which M increases linearly with a slope of 0.013 μ_B/T/Co^{2+} due to the Van Vleck paramagnetism. The saturation magnetization, $M_s = 2.1$ μ_B/Co^{2+}, is obtained by the extrapolation of the magnetization curve from well above the saturation field. This value is similar to the M_s of $Ba_3CoSb_2O_9$ [3], which can be obtained from a S-1/2 spin state with $g = 3.84$ due to the spin-orbital coupling. The $M(H)$ curve shows weak changes of slope below H_s.

The weak changes of the slope are more evident in the first derivative of the magnetization curves (dM/dH) as peaks and valleys [Fig. 4(a)]. The field dependence of the ac magnetic susceptibility data $[\chi'(H)]$ show similar features of the peaks and valleys as well as the overall shape. The similarity between is expected because χ' can probe dM/dH directly and allows one to use χ' to identify magnetization

TABLE I. Structural and magnetic parameters obtained by the Rietveld refinement for the NPD pattern at $T = 0.24$ K.

Atoms	X	Y	Z
Ba1	0.0000	0.0000	0.0000
Ba2	0.3333	0.6667	0.6613 ± 0.0014
Co1	0.0000	0.0000	0.5000
Nb1	0.3333	0.6667	0.1751 ± 0.0012
O1	0.5000	0.0000	0.0000
O2	0.1677 ± 0.0010	0.3353 ± 0.0020	0.3319 ± 0.0009
Space group	Lattice parameters (Å)	RF factor	Bragg R factor
P-3m1	$a = 5.7703(1)$ $b = 5.7703(1)$ $c = 7.0808(3)$ $\alpha = \beta = 90°$ $\gamma = 120°$	4.16	3.09
Magnetic space group	Momentum		
P-1	0.97(1)		

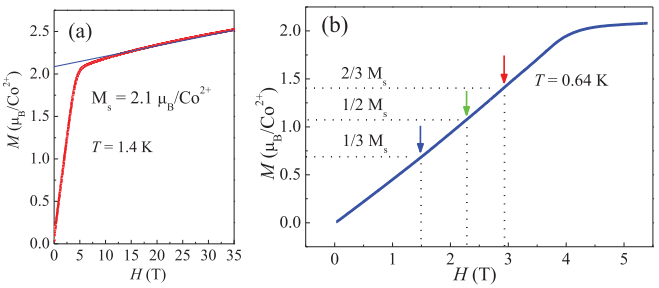

FIG. 3. (Color online) (a) The high-field dc magnetization data at $T = 1.4$ K up to $H = 35$ T (a) and at $T = 0.64$ K between 0 and 5.5 T (b). The arrows indicate the transitions explained in the text.

changes with higher resolution. The oscillatory features can be even more clearly detected by subtracting the background (empirical linear background) as shown in Fig. 5.

Both the dM/dH and χ' data show series of oscillatory features at consistent field positions. For dM/dH at 0.64 K, these field positions are 1.41(17) T, 2.22(12) T, and 3.08(8) T. It is notable that the magnetization values at these three field positions of the valleys are close to 1/3, 1/2, and 2/3 (or $\sqrt{3}/3$) of M_s, respectively. All these features imply a series of magnetic phase transitions with increasing field and the fractional magnetization values can be used to deduce the magnetic phases at different fields. We indicate the field

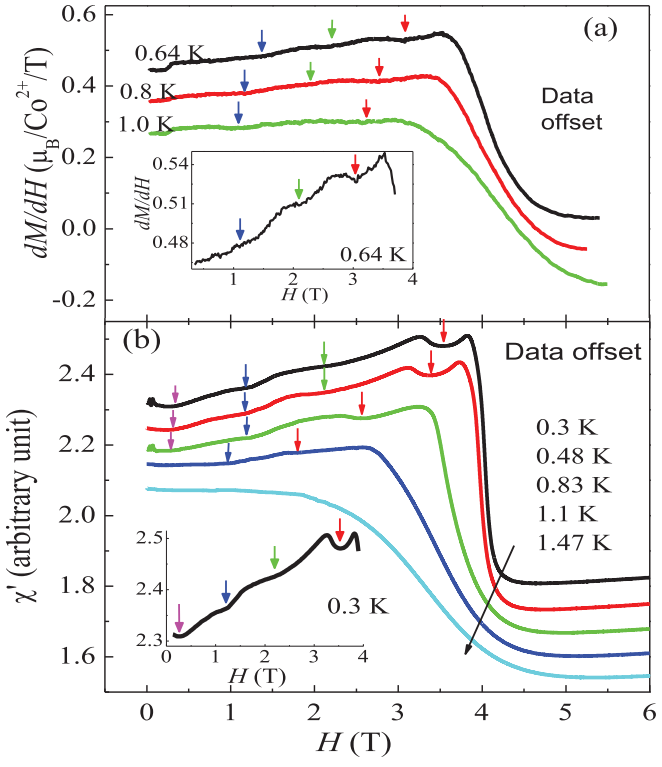

FIG. 4. (Color online) (a) The first derivative of the dc magnetization as a function of field at different temperatures. Data are offset by $-0.1\ \mu_B/Co^{2+}/T$ from 0.64 K data incrementally. Inset: Enlargement of the 0.64 K data at low fields. (b) The dc magnetic field dependence of χ' at different temperatures. Data are offset by -0.07 from 0.3 K data. Inset: Enlargement of the 0.3 K data at low fields. The arrows indicate the transitions explained in the text.

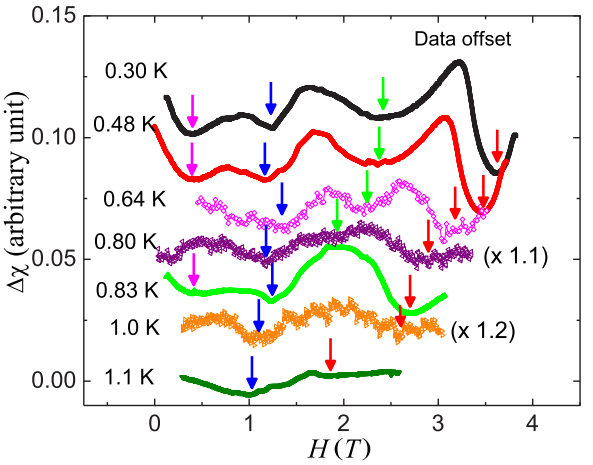

FIG. 5. (Color online) Oscillatory components of χ' (solid symbols) and dM/dH (empty symbols) obtained by subtracting empirical linear backgrounds. The arrows indicate the same transitions shown in Fig. 4.

positions of the valleys as down arrows, and will use these field positions to build a phase diagram later [26].

The temperature dependence of χ' (see Fig. 6) also reveals a two-step transition at T_{N1} (red arrows) and T_{N2} (black arrows). The temperature dependencies of $\chi'(T)$ at $H = 0$ and 2 T are similar to those of the dc magnetic susceptibility $[\chi(T)]$ data measured at $H = 0.1$ T and 2 T. The similarity suggests a nonglassy magnetic system and allows us systematic studies of the magnetic field dependence of the transitions. With increasing magnetic fields, the features related to the two-step transition shift to low temperatures and become weaker, and only one transition is observed above $H = 3$ T in the measured temperature range. The position of the transition is assigned to the peak or to the temperature where the high-temperature extrapolation deviates as shown in the inset of Fig. 6(b).

D. Dielectric constant and polarization

Figure 7 shows the temperature dependence of the dielectric constant ε' at different fields. At zero field, two anomalies, a slope change around 1.4 K and a sharp peak at around 1.1 K, were observed with overall tendency of monotonically increasing behavior. Here, we focus only on the anomalies as they are related to the phase transitions and treat the overall increase of the dielectric constant as background. As the magnetic field increases, both anomalies become weaker and shift to lower temperatures. At a certain range of field, between 2.75 and 3.25 T, an additional smaller peak (indicated as an asterisk) was observed at a slightly higher temperature than that of the larger peak. The peak temperatures were extracted by fitting the curves with independent Gaussian functions after the background (ε_{bkg}) was subtracted. For example, Fig. 8 shows $\Delta\varepsilon$ ($=\varepsilon - \varepsilon_{bkg}$) at $H = 1$ and 3.25 T and the Gaussian fitting curves. The peak temperatures are indicated as arrows and asterisks.

The field dependence of ε' also shows several features as peaks and valleys, while ε' increases monotonically above H_s. Their field positions are indicated by down arrows and as asterisks as shown in Fig. 9. All these features are closely correlated to the features observed by the dc and ac

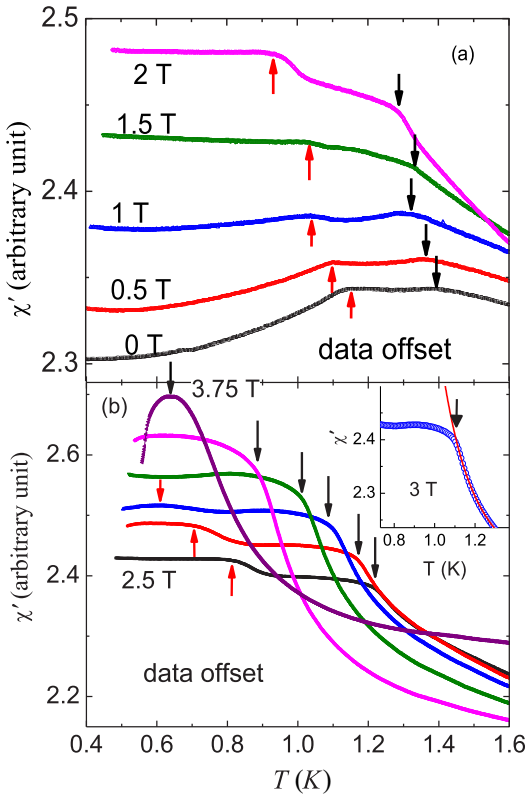

FIG. 6. (Color online) (a) Temperature dependence of the ac magnetic susceptibility (χ') at low fields (0–2 T) (a) and at higher fields (3.75, 3.5, 3.25, 3, 2.75, 2.5 T from the top) (b). Data are offset incrementally by 0.02 from 0 T data (a) and 0.04 from 2.5 T data (b), respectively. The arrows indicate the transitions explained in the text. The inset of (b) is the detailed view of 3 T data near the high-temperature transition to show how T_{N2} was determined. The solid line is the third-order inverse polynomial fitting of the high-temperature data.

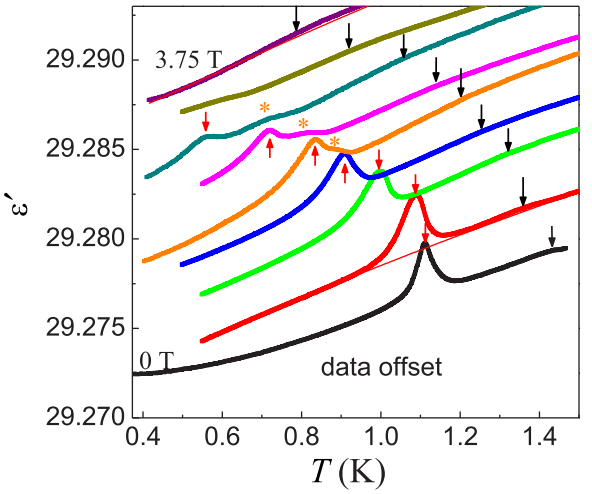

FIG. 7. (Color online) Temperature dependence of the dielectric constant (ε') at different fields of $H = 3.75$, 3.5, 3.25, 3.0, 2.75, 2.5, 2.0, 1.0, and 0 T from top to bottom. Data are offset by 0.001 incrementally from 0 T data. The solid lines are examples of the empirical background (third-order polynomial fitting) curves for $H = 1$ and 3.75 T data. The arrows and asterisks indicate the transitions explained in the text.

magnetic measurements, which again support the occurrence of a series of magnetic phase transitions. For example, at similar temperatures, the field positions (from low to high field) for the first peak, the valley, and the second peak shown by the $\varepsilon'(H)$ curves are consistent with the field positions (from low to high field) for the first, second, and fourth valley shown by the $\chi'(H)$ curves. The small features indicated as asterisks are originated from the same phenomena observed from the temperature sweeps (asterisks in Figs. 7 and 8), which are more clearly seen after the smoothly varying backgrounds are removed (see the inset of Fig. 9).

In general, dielectric constant anomalies can be observed from phase transitions associated with different order parameters, i.e., lattice (structural phase transition), polarization [para-(anti)ferroelectric transition] and magnetization (magnetic phase transition via magnetoelectric effect). It is possible that more than one order parameter (e.g., polarization and magnetization) are involved in the transition as in magnetic multiferroics. To investigate such possibilities, we performed polarization measurements.

Figures 10(a) and 10(b) show pyroelectric current (I_p) and corresponding polarization (P) data taken at 0, 2, and 3 T. The polarization can be only observed when the sample is cooled under electric field (poling) and its sign depends on the sign of the electric field, thus indicating spontaneous and reversible characteristics. On the other hand, the polarization is independent of the presence of magnetic field during the cool down process, i.e., independent of magnetoelectric annealing. The magnetoelectric annealing could make a difference if the transition were purely magnetic in origin as observed in some magnetoelectric materials [27].

The reversible and spontaneous polarization suggests the ferroelectric (FE) ground state at low temperatures, hence multiferroicity in $Ba_3CoNb_2O_9$. At zero field, P is observed to increase in two-step processes, a small increase at 1.4 K and a rapid increase at 1.1 K, which are consistent with the values of T_{N2} and T_{N1}. The polarization appears up to 3 T with increasing field but the transition becomes weaker and broadened. The magnitude of the polarization is three times smaller than its sister compound $Ba_3NiNb_2O_9$, which made it difficult to study the ferroelectric order parameter (P) in more detail.

IV. DISCUSSION

An H-T phase diagram [Fig. 11(a)] is constructed by combining all the data shown above. Each symbol represents different experimental techniques, whose position corresponds to the arrows and the asterisks in Figs. 1–10. The positions are obtained either by estimating the deviation temperature from the high-temperature extrapolation [e.g., inset of Fig. 6(b)] or by fitting with the Gaussian function (e.g., Figs. 7 and 8). The former method was used for $\chi'(T)$, NPD, and $I_p(T)$ data, and the latter for the others. A simplified version without individual data points is shown in Fig. 11(b). In addition to the high-temperature paramagnetic (PM) and paraelectric (PE) state, we consistently identified six different phases from different measurements. They are labeled as A, A′, B, B′, C, and C′. We have assigned the A′-B, B-B′, B′-C phase boundaries by

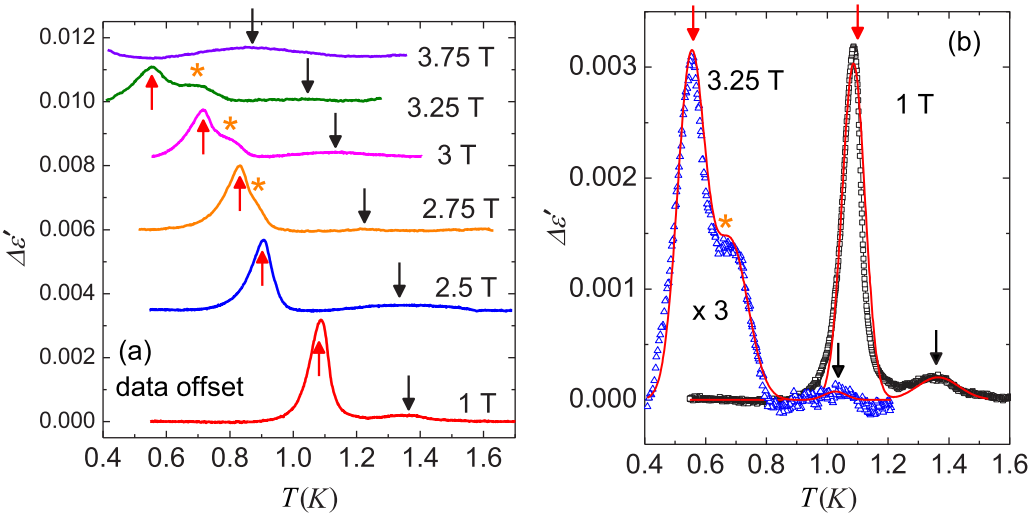

FIG. 8. (Color online) (a) Temperature dependence of the dielectric constant at different fields after the background is removed. (b) Expansion of $H=$ 1 and 3.25 T data. The solid lines are Gaussian fitting curves. The arrows and asterisks indicate the transitions shown in Fig. 7.

referencing the magnetization values of Fig. 3(b) at fields and temperatures of the phase boundaries, which are 1/3, 1/2, and 2/3 (or $\sqrt{3}/3$) of M_s, respectively. In most cases, both magnetic (M, χ, χ') and electric (ε', P) probes result in the same phase boundaries due to the multiferroicity. Exceptions can be found in C-C′ and B-B′ phase boundaries where only electric or magnetic probes revealed phase transitions. The two-step process of the polarization and its appearance under fields indicate that the FE state survives for all magnetic ordered phases. Therefore, the PE-FE phase boundary follows the PM/PE-C boundary.

At zero field, all different measurements consistently show that $Ba_3CoNb_2O_9$ goes through a two-step transition at $T_{N2} =$ 1.36 K and $T_{N1} = 1.10$ K. The temperature dependence of the order parameter [Fig. 2(b)] suggests that T_{N1} is the temperature below which the system enters a 120° AFM phase (A phase). For a Heisenberg model with an easy-axis exchange anisotropy, the *uud* phase has been predicted to extend to $H = 0$ [28,29], and an easy-axis single-ion anisotropy has been shown to stabilize *uud*-like phases at $H = 0$ [30], as

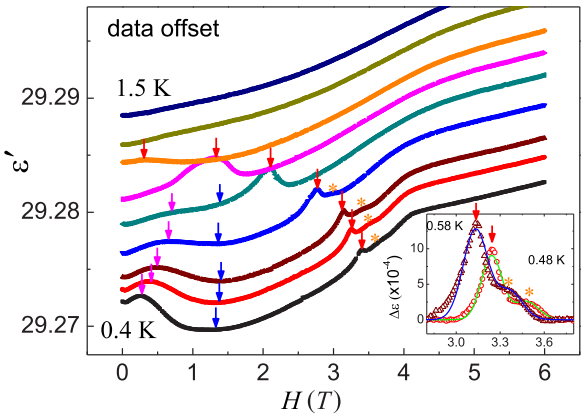

FIG. 9. (Color online) Field dependence of ε' at different temperatures of $T = 1.5$, 1.32, 1.15, 1.05, 0.94, 0.77, 0.58, 0.48, and 0.4 K from top to bottom. Data are offset by 0.001 incrementally from the 0.4 K data. Inset: Expansion around $H = 3.25$ T data at $T = 0.48$ K and 0.58 K after the background is removed. The arrows and asterisks indicate the transitions explained in the text.

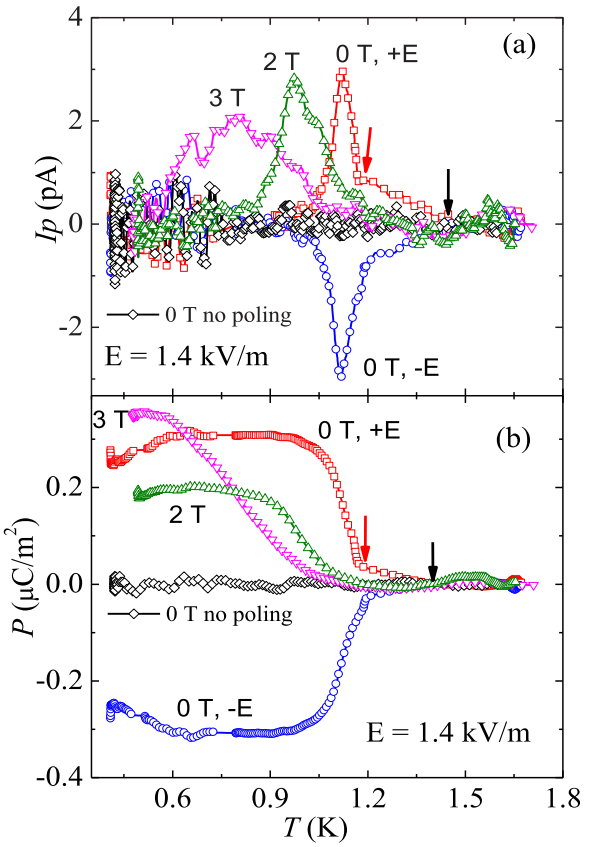

FIG. 10. (Color online) (a) Pyroelectric current (I_p) measured under different poling fields and magnetic fields. (b) Polarization data obtained from integration of I_p shown in (a). The arrows and asterisks indicate the transitions explained in the text.

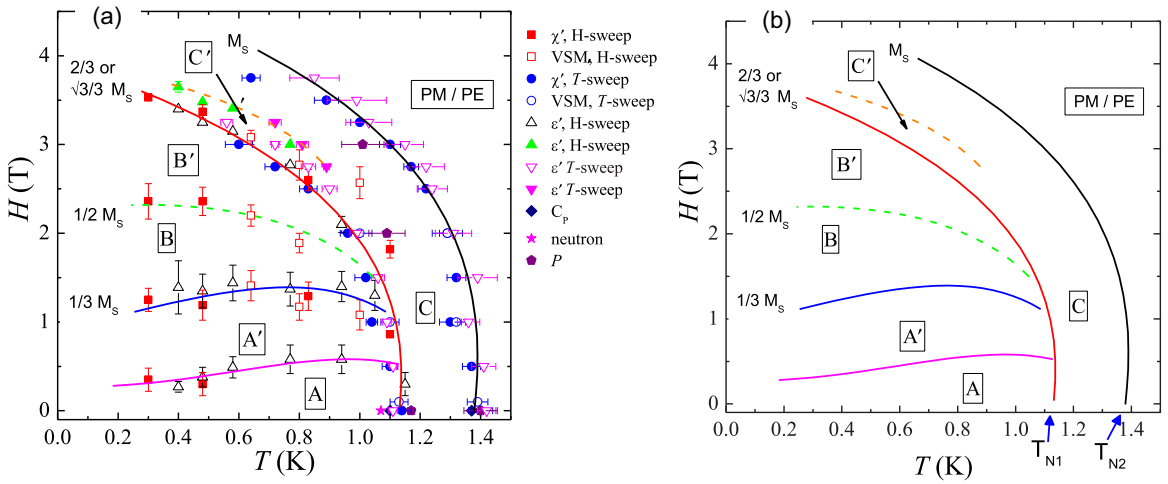

FIG. 11. (Color online) The H-T phase diagram (a) with individual data points obtained from the experimental techniques shown in the legend and (b) in a simplified form without the data points. The lines are guides to eyes. The color of each line matches the color of the arrows used in Figs. 1–10, whose field or temperature positions were used to build the phase diagram. The solid (dashed) lines represent the phase boundaries determined by both (either) magnetic and (or) electric probes. The error bars are determined from the procedures of extracting peak or valley positions (standard deviation of the Gaussian distribution) or estimating the deviation temperature (the uncertainty of the the high-temperature extrapolation fitting).

observed for $Rb_4Mn(MoO_4)_3$ (S-5/2) [10]. By contrast, the *uud* phase appears to be either absent or very narrow at $H = 0$ for the isotropic Heisenberg model [31–33]. The two-step transition for $Ba_3CoNb_2O_9$ indicates the possible existence of easy-axis anisotropy in the system. Due to the crystal field and spin-orbital coupling, it is actually normal for the Co^{2+} ions on octahedral sites to show easy-axis anisotropy. For example, the neutron diffraction results on $Ba_3CoSb_2O_9$ suggested a 120° structure with one spin along the c axis [24]. For $ACoB_3$, they are Ising antiferromagnets with spins lying parallel or antiparallel to the c axis due to strong easy-axis anisotropy [25]. Here, one thing that has to be emphasized is that although the spin structure between T_{N1} and T_{N2} was not clearly resolved by our neutron diffraction measurements, the phase boundary reference indicates that the C phase between T_{N1} and T_{N2} at zero field is the phase with 2/3 (or $\sqrt{3}/3$) M_s. Therefore, $Ba_3CoNb_2O_9$ enters the C phase and then the 120° (A) phase upon cooling at zero field; this is different from the theoretical prediction that the TLAFs will first enter the *uud* phase (or the B phase for $Ba_3CoNb_2O_9$) and then enter the 120° phase. This discrepancy needs further studies to be clarified.

Theoretical studies have predicted that for TLAFs with quantum spins, the quantum spin fluctuations can stabilize the *uud* phase over a certain range of magnetic field showing a magnetization plateau with a value of 1/3 M_s at zero temperatures [6,34–36], as observed in Cs_2CuBr_4 (S-1/2) [13,14], $Ba_3CoSb_2O_9$ (S-1/2) [3,4,5], $Ba_3NiSb_2O_9$ (S-1) [11], and $Ba_3NiNb_2O_9$ (S-1) [12]. For TLAFs with classical spins, both an easy-axis exchange anisotropy and an easy-axis single-ion anisotropy can make the *uud* phase survive down to zero temperature [29], as observed in $Rb_4Mn(MoO_4)_3$ [10]. More interestingly, the recent studies on TLAFs (e.g., 1/2, 5/9, 2/3 M_s in Cs_2CuBr_4 [14], 3/5 M_s in $Ba_3CoSb_2O_9$ [4]) revealed that there are more spin states with higher M values than 1/3 M_s under magnetic fields. Although there is no full understanding of these spin states yet, one common agreement is that the strong quantum fluctuations play an important role for stabilizing the series of quantum spin states, considering that all the experimental observations of these extra spin states were made from TLAFs with S-1/2. Here, our studies on $Ba_3CoNb_2O_9$ show that it is a rare example of a TLAF exhibiting a series of spin states with fractional magnetization as 1/3M_s (B phase), 1/2 M_s (B′ phase), and 2/3 M_s (or $\sqrt{3}/3$ M_s, C phase). These spin states are very similar to those observed in Cs_2CuBr_4. Our experimental resolution cannot make a difference between 2/3 M_s and $\sqrt{3}/3$ M_s. For $Ba_3CoNb_2O_9$, the possible easy-axis anisotropy could play a role for the stabilization of the *uud* phase, but the strong quantum spin fluctuations for S-1/2 should be the main factor leading to the series of quantum spin states.

Here we want to point out that to observe the magnetization plateau, the external magnetic field should be applied along a certain direction of single-crystalline samples [4,10,19]. The magnetization plateau can be also observed in powder samples due to the random orientation of the crystal orientation in the polycrystalline sample. But due to the averaging effect, the dM/dH can be smaller in polycrystalline samples and the magnetization plateau can be not as obvious as in single-crystal samples [3,11]. The typical dM/dH curve near the magnetization plateau region shows a U-shaped broad valley with two sharp peaks at entering and exiting the plateau region [3,9,10]. In $Ba_3CoNb_2O_9$, the magnetization plateau was not clearly observed, which is probably due to the polycrystalline nature of the sample in our work. Nevertheless, the peak-valley-peak feature of dM/dH at the magnetic field where the magnetization is close to 1/3 M_s is suggestive of the 1/3 M_s magnetization plateau. Similar situations occur for the 1/2 M_s and 2/3 M_s (or $\sqrt{3}/3$ M_s) cases.

Another two noteworthy features for the phase diagram are that (i) there is an A′ phase between the A (120° structure) and B (*uud*) phases. Normally, with increasing field the 120° phase directly enters the *uud* phase, as shown by all other

TLAFs mentioned above. The A′ phase observed here could be a new spin flop phase with spins canted from the 120° structure but without the up-up-down configuration. This also suggests that the 120° is not stable up to the *uud* phase in $Ba_3CoNb_2O_9$. (ii) The C′ phase boundary is just observed from the dielectric constant measurements; whether it represents a true phase transition needs further studies to be clarified.

At the end, we compare $Ba_3CoNb_2O_9$ to $Ba_3NiNb_2O_9$, both of which are rare TLAFs showing coexistence of successive magnetic phase transitions and multiferroicity. The comparisons show that (i) the multiferroicity in $Ba_3CoNb_2O_9$ is similar to what was found in $Ba_3NiNb_2O_9$; i.e., the FE phase exists both in collinear and noncollinear spin states. Therefore, the symmetry argument and the speculation for the FE origin can be applied to both compounds as stated in Ref. [13]. This is somewhat expected since the two compounds are exactly of same structure and share similar magnetic phases. Here we provide one more rare example of a TLAF with S-1/2 to confirm the prediction that multiferroicity can be found in a wide range of trigonal materials with 120° spin structure [20]. (ii) Apparently, $Ba_3CoNb_2O_9$ has a more complicated H-T phase diagram with the existence of the additional primed phase. $Ba_3NiNb_2O_9$ shows a one-step transition at zero field and simpler $1/3M_s$ and $\sqrt{3}/3$ M_s phase boundaries under fields. The complex magnetic phases of the Co sample should originate from the possible easy-axis anisotropy and the stronger quantum fluctuations with smaller spin S-1/2. Presumably, easy-axis anisotropy does not exist in the Ni sample.

In summary, although more work is needed to confirm the magnetic structures of all phases, the detailed magnetic and electric studies on $Ba_3CoNb_2O_9$ reveal that (i) It is a rare quasi-two-dimensional TLAF with effective S-1/2 showing complex magnetic phase transitions among phases with fractional magnetization as 1/3, 1/2, and 2/3 (or $\sqrt{3}/3$) M_s. It provides another rare example showing that strong quantum fluctuations on a triangular lattice possibly lead to more quantum spin states than the theoretically predicted *uud* state. (ii) It is multiferroic for all the ordered magnetic phases regardless of the spin chirality, which is similar to the multiferroicity in the isostructural $Ba_3NiNb_2O_9$. The results show the robustness of the multiferroicity in this class of material.

ACKNOWLEDGMENTS

We thank P. Schlottmann for useful discussions and Tim Murphy, Ju-Hyun Park, and Glover Jones for their help with experiments carried out at the NHMFL. Z.L.D. and H.D.Z. thank for the support of JDRD program of University of Tennessee. The NHMFL is supported by NSF-DMR-1157490 and the State of Florida and by the additional funding from NHMFL User Collaboration Support Grant. X.K. acknowledges the financial support from the start-up funds at Michigan State University. A portion of this research at ORNL High Flux Isotope Reactor was sponsored by the Scientific User Facilities Division, Office of Basic Energy Sciences, US Department of Energy.

[1] L. Balents, Nature (London) **464**, 199 (2010).
[2] A. P. Ramirez, Annu. Rev. Mater. Sci. **24**, 453 (1994).
[3] Y. Shirata, H. Tanaka, A. Matsuo, and K. Kindo, Phys. Rev. Lett. **108**, 057205 (2012).
[4] T. Susuki, N. Kurita, T. Tanaka, H. Nojiri, A. Matsuo, K. Kindo, and H. Tanaka, Phys. Rev. Lett. **110**, 267201 (2013).
[5] H. D. Zhou, Cenke Xu, A. M. Hallas, H. J. Silverstein, C. R. Wiebe, I. Umegaki, J. Q. Yan, T. P. Murphy, J. H. Park, Y. Qiu, J. R. D. Copley, J. S. Gardner, and Y. Takano, Phys. Rev. Lett. **109**, 267206 (2012).
[6] A. V. Chubukov and D. I. Golosov, J. Phys.: Condens. Matter **3**, 69 (1991).
[7] S. Miyahara, K. Ogino, and N. Furukawa, Physica B **378–380**, 587 (2006).
[8] J. Alicea, A. V. Chubukov, and O. A. Starykh, Phys. Rev. Lett. **102**, 137201 (2009).
[9] A. I. Smirnov, H. Yashiro, S. Kimura, M. Hagiwara, Y. Narumi, K. Kindo, A. Kikkawa, K. Katsumata, A. Ya. Shapiro, and L. N. Demianets, Phys. Rev. B **75**, 134412 (2007).
[10] R. Ishii, S. Tanaka, K. Onuma, Y. Nambu, M. Tokunaga, T. Sakakibara, N. Kawashima, Y. Maeno, C. Broholm, D. P. Gautreaux, J. Y. Chan, and S. Nakatsuji, Europhys. Lett. **94**, 17001 (2011).
[11] Y. Shirata, H. Tanaka, T. Ono, A. Matsuo, K. Kindo, and Hiroki Nakano, J. Phys. Soc. Jpn. **80**, 093702 (2011).
[12] J. Hwang, E. S. Choi, F. Ye, C. R. Dela Cruz, Y. Xin, H. D. Zhou, and P. Schlottmann, Phys. Rev. Lett. **109**, 257205 (2012).
[13] T. Ono, H. Tanaka, H. Aruga Katori, F. Ishikawa, H. Mitamura, and T. Goto, Phys. Rev. B **67**, 104431 (2003).
[14] N. A. Fortune, S. T. Hannahs, Y. Yoshida, T. E. Sherline, T. Ono, H. Tanaka, and Y. Takano, Phys. Rev. Lett. **102**, 257201 (2009).
[15] Y. Tokura, Science **312**, 1481 (2006).
[16] K. F. Wang, J.-M. Liu, and Z. F. Ren, Adv. Phys. **58**, 321 (2009).
[17] N. A. Spaldin and M. Fiebig, Science **309**, 391 (2005).
[18] W. Eerenstein, N. D. Mathur, and J. F. Scott, Nature (London) **442**, 759 (2006).
[19] L. E. Svistov, A. I. Smirnov, L. A. Prozorova, O. A. Petrenko, L. N. Demianets, and A. Ya. Shapiro, Phys. Rev. B **67**, 094434 (2003).
[20] S. Seki, Y. Onose, and Y. Tokura, Phys. Rev. Lett. **101**, 067204 (2008).
[21] K. Kimura, H. Nakamura, K. Ohgushi, and T. Kimura, Phys. Rev. B **78**, 140401(R) (2008).
[22] H. J. Xiang, E. J. Kan, Y. Zhang, M.-H. Whangbo, and X. G. Gong, Phys. Rev. Lett. **107**, 157202 (2011).
[23] V. Ting, Y. Liu, L. Noren, R. L. Withers, D. J. Goossens, M. James, and C. Ferraris, J. Solid State Chem. **177**, 4428 (2004).
[24] Y. Doi, Y. Hinatsu, and K. Ohoyama, J. Phys.: Condens. Matter **16**, 8923 (2004).
[25] M. F. Collins and O. A. Petrenko, Can. J. Phys. **75**, 605 (1997).
[26] The valleys of dM/dH are chosen because they represent where the field dependence is the smallest. The other experimental results in this work are also more consistent with positions of the valleys.

[27] G. T. Rado and V. J. Folen, Phys. Rev. Lett. **7**, 310 (1961).
[28] S. Miyashita and H. Kawamura, J. Phys. Soc. Jpn. **54**, 3385 (1985).
[29] S. Miyashita, J. Phys. Soc. Jpn. **55**, 3605 (1986).
[30] P.-É. Melchy and M. E. Zhitomirsky, Phys. Rev. B **80**, 064411 (2009).
[31] H. Kawamura and S. Miyashita, J. Phys. Soc. Jpn. **54**, 4530 (1985).
[32] M. V. Gvozdikova, P.-E. Melchy, and M. E. Zhitomirsky, J. Phys.: Condens. Matter **23**, 164209 (2011).
[33] L. Seabra, T. Momoi, P. Sindzingre, and N. Shannon, Phys. Rev. B **84**, 214418 (2011).
[34] A. Honecker, J. Phys.: Condens. Matter **11**, 4697 (1999).
[35] D. J. J. Farnell, R. Zinke, J. Schulenburg, and J. Richter, J. Phys.: Condens. Matter **21**, 406002 (2009).
[36] T. Sakai and H. Nakano, Phys. Rev. B **83**, 100405(R) (2011).